Chemical Science

ROYAL SOCIETY OF CHEMISTRY

EDGE ARTICLE

View Article Online
View Journal | View Issue

Cite this: *Chem. Sci.*, 2023, **14**, 1524

All publication charges for this article have been paid for by the Royal Society of Chemistry

Received 1st December 2022
Accepted 12th January 2023

DOI: 10.1039/d2sc06629g

rsc.li/chemical-science

Maximized axial helicity in a Pd_2L_4 cage: inverse guest size-dependent compression and mesocate isomerism†‡

Witold M. Bloch, *[ab] Shinnosuke Horiuchi, [ac] Julian J. Holstein, [a] Christoph Drechsler,[a] Axel Wuttke,[d] Wolf Hiller, [a] Ricardo A. Mata [d] and Guido H. Clever *[a]

Helicity is an archetypal structural motif of many biological systems and provides a basis for molecular recognition in DNA. Whilst artificial supramolecular hosts are often helical, the relationship between helicity and guest encapsulation is not well understood. We report a detailed study on a significantly coiled-up Pd_2L_4 metallohelicate with an unusually wide azimuthal angle (~176°). Through a combination of NMR spectroscopy, single-crystal X-ray diffraction, trapped ion mobility mass spectrometry and isothermal titration calorimetry we show that the coiled-up cage exhibits extremely tight anion binding (K of up to 10^6 M^{-1}) by virtue of a pronounced oblate/prolate cavity expansion, whereby the Pd–Pd separation decreases for mono-anionic guests of increasing size. Electronic structure calculations point toward strong dispersion forces contributing to these host–guest interactions. In the absence of a suitable guest, the helical cage exists in equilibrium with a well-defined mesocate isomer that possesses a distinct cavity environment afforded by a doubled Pd–Pd separation distance.

Introduction

The prevalence of structural helicity in biological systems exemplifies its fundamental importance for complex functions. For example, the helical structure of DNA provides a chiral surface for recognition and facilitates tight packing of genetic information.[1] Coiled motifs in peptide chains, such as α-helices, experience strong structural reinforcement through cooperative non-covalent interactions, giving rise to a stiff secondary structure. Clearly, helicity is important for defining the tertiary structure and biological function of proteins and other biomacromolecules.[2]

These findings have inspired chemists to prepare artificial assemblies with structural helicity as the blueprint, such as helical molecules,[3,4] foldamers[5,6] and polymer aggregates.[7] Many of these helical assemblies find strong applications in various areas, including asymmetric catalysis[8] and biomedicine.[9] For example, dinuclear metallohelicates composed of two or three twisted ligand strands have been shown to inhibit malignant cell growth by binding the major groove of DNA.[10–12]

The family of quadruple-stranded metallohelicates intersects with the compound class of M_2L_4 coordination cages, the former defined by a helical twist, the latter by an accessible cavity.[13,14] The degree of axial helicity for M_2L_4 lantern-shaped cages can be defined by the azimuthal angle, α, which is the angular projection of the bridging ligand respective to the metal–metal axis (Fig. 1a).[15] Many non-helical M_2L_4 cages (Fig. 1b) have shown promising functions for molecular separation,[16,17] anion sequestration,[18,19] catalysis[20,21] and drug delivery.[22–24] Despite helicity being a functional motif in nature, efforts to augment the host–guest chemistry of M_2L_4 cages have mainly focused on increasing their structural complexity.[25] The incorporation of functional ligands (chiral, photo-switchable, redox-active, *etc.*) into such cage architectures offers the prospect of multi-functionalisation through heteroleptic, heterometallic or other low-symmetry assembly approaches.[25–34] Moreover, structural motifs such as skewed geometry and double-cage interpenetration have been shown to give rise to phenomena such as shape recognition, allosteric binding and stimuli responsiveness.[35–38]

The relationship between axial helicity and the guest binding properties of M_2L_4 coordination cages is somewhat ill-defined.[19]

[a]*Department of Chemistry and Chemical Biology, TU Dortmund University, Otto-Hahn-Straße 6, 44227 Dortmund, Germany. E-mail: guido.clever@tu-dortmund.de*

[b]*Institute for Nanoscale Science and Technology, College of Science and Engineering, Flinders University, Adelaide, South Australia 5042, Australia. E-mail: witold.bloch@flinders.edu.au*

[c]*Division of Chemistry and Materials Science, Graduate School of Engineering, Nagasaki University, Bunkyo-machi, Nagasaki, 852-8521, Japan*

[d]*Institute of Physical Chemistry, Georg-August University Göttingen, Tammannstraße 6, 37077 Göttingen, Germany*

† Dedicated to Professor Peter Steel on the occasion of his 68th birthday.

‡ Electronic supplementary information (ESI) available: Full experimental details and supporting analysis. CCDC 1851098–1851104. For ESI and crystallographic data in CIF or other electronic format see DOI: https://doi.org/10.1039/d2sc06629g

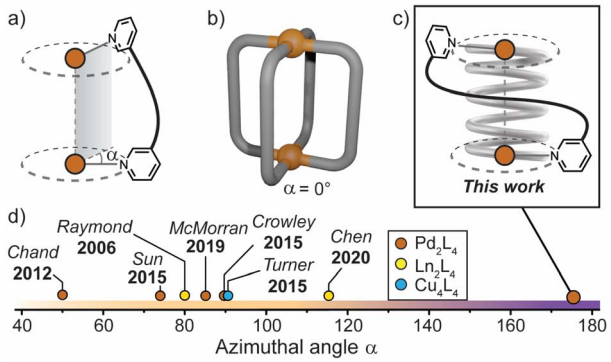

Fig. 1 (a) Azimuthal angle (α) for a M_2L_4 helicate; (b) general structure of a non-helical M_2L_4 cage, where $\alpha = 0°$; (c) this work: a tightly-wrapped Pd_2L_4 helicate that behaves as a supramolecular spring; (d) azimuthal angles (extracted from X-ray diffraction data) of selected quadruple-stranded metallohelicates, shown for comparison.[15,39,42–46]

McMorran and Steel demonstrated that a helical $Pd_2\mathbf{L}_4$ cage assembled from flexible 4-bis(3-pyridyloxy)benzene ligands undergoes cavity adaptation by increasing its Pd–Pd separation and helical pitch upon binding anionic guests of increasing size.[13,39] Jung and Lee demonstrated that a non-helical $Pd_2\mathbf{L}_4$ cage assembled from alkyl-derived ligands behaves in a similar fashion, whereby an increase in the Pd–Pd separation is observed when the cage binds anions of increasing size.[40] It is therefore unclear whether axial helicity or ligand flexibility is primarily responsible for mediating cavity expansion in M_2L_4 coordination cages.

In these and related M_2L_4 cages, the equilibrium constant for anion binding in polar solvents is rather low ($<10^3\ M^{-1}$) leading to the necessity of utilising non-polar solvents to achieve stronger host–guest interactions.[41] Moreover, the azimuthal angle (α) of so far reported helical M_2L_4 cages ($M = Pd^{II}$, Pt^{II} or lanthanides) has been largely limited to $\leq 90°$ (Fig. 1d); increasing α beyond this limit represents uncharted territory for M_2L_4 cages. We postulated that maximising the axial helicity of M_2L_4 cages will lead to enhanced guest binding properties (compared to cages where $\alpha \leq 90°$) as the tightly-wrapped ligands should provide a large internal surface area and disfavour guest unbinding.

Herein, we report a $Pd_2\mathbf{L}_4$ helical cage (**1**) with azimuthal angles ranging between 171–176° (Fig. 1c and d), representing the most axially-twisted M_2L_4 coordination cage reported so far. We closely examine the cage's unique structural changes associated with the binding of mono-anions through extensive X-ray crystallographic, NMR, MS and ITC analyses, as well as electronic structure calculations. Together, these experiments provide intimate structural details on the pronounced host–guest adaptability of **1**, facilitated by its significantly twisted, spring-like architecture. In addition, we probe the anion-dependent equilibrium between the coiled-up metallohelicate and its elongated mesocate isomer, which is a unique feature of this system. Together, these findings provide new detailed insights into the relationship between axial helicity, structural adaptability and guest-binding phenomena of artificial host assemblies.

Results and discussion

Ligand design

To prepare a coordination cage with an azimuthal angle of >90°, we designed a bis-monodentate ligand with a carbazole backbone and two inward-pointing 8-substituted isoquinoline donors (**L**).[35] This pincer-shaped ligand has a theoretical ligand bite angle of 15° (Fig. 2a) as defined by the intersection of a vertical vector along the ligand backbone and one running parallel to the N-donor.[47] Given the rigidity of **L** and the necessity of adopting a bite angle of ~90° for lantern-shaped M_2L_4 coordination cages (particularly with square-planar Pd^{II}), we anticipated that the isoquinoline donors of **L** would need to undergo severe twisting to bridge two Pd^{II} ions. **L** was synthesized through a Sonogashira cross-coupling between 3,6-dibromo-9-hexyl-9*H*-carbazole and 8-ethynylisoquinoline in 53% yield (ESI†).

Synthesis and solution-state analysis of 1·X

Heating a 2 : 1 mixture of **L** with $[Pd(CH_3CN)_4](BF_4)_2$ at 70 °C in CD_3CN resulted in the assembly of the coordination cage $[BF_4@Pd_2\mathbf{L}_4](BF_4)_3$ (herein denoted as $\mathbf{1}\cdot\mathbf{BF_4}$) as revealed by ^1H NMR spectroscopy and electrospray ionisation mass spectrometry (ESI-MS). In the ^1H NMR spectrum, the proton

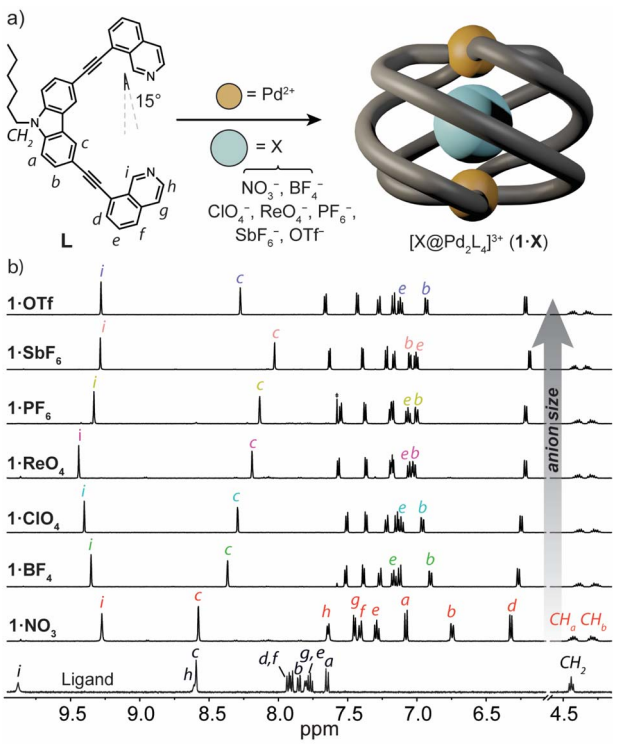

Fig. 2 (a) A scheme showing the structure and native bite angle of **L** and its self-assembly with Pd^{II} to give the $Pd_2\mathbf{L}_4$ helicate **1·X**, where X = different anionic guests; (b) ^1H NMR spectra (500 MHz/CD_3CN) of ligand **L** (bottom) and **1·X** (top).

resonances of the cage are significantly upfield-shifted relative to **L** (Fig. 2b), consistent with the presence of π-stacking interactions between neighbouring ligands in the cage assembly. The characteristic splitting of the diastereotopic *N*-hexyl CH_2 resonances (CH_a, CH_b, 4.18–4.48 ppm at 298 K) provides direct evidence for axial helicity, and the *P* and *M* enantiomers of the $Pd_2\mathbf{L}_4$ cage are in slow exchange relative to the ^{1}H NMR time scale. The encapsulation of a BF_4^- anion within **1** was confirmed by ^{19}F NMR spectroscopy, which revealed two resonances at −151.8 ppm and −149.4 ppm (Fig. S10†). These are assigned to the free and tightly encapsulated BF_4^- anion, respectively, and ^{19}F exchange spectroscopy (EXSY) confirmed their exchange at 25 °C (Fig. S15†).

Next, we examined the self-assembly of **1** in the presence of anionic guests of different size and shape. We prepared a series of cage analogues (**1·X**), either from the respective Pd^{II} salt (X = NO_3^-, ClO_4^-, PF_6^-, SbF_6^- and OTf^-), or by anion exchange (X = ReO_4^-). ESI-MS confirmed the $Pd_2\mathbf{L}_4$ assembly for each counterion by prominent signals corresponding to $[Pd_2\mathbf{L}_4 + n\mathrm{X}]^{(4-n)+}$ cations; n = 1 and 2 (ESI†). When comparing their ^{1}H NMR spectra, the hydrogens that point directly into the cage cavity appear at distinct chemical shifts (see resonances *c* and *i*, Fig. 2b). As for **1·BF$_4$**, also for **1·PF$_6$** and **1·OTf**, ^{19}F NMR spectroscopy confirmed anion encapsulation, indicating that the cage cavity can accommodate anions of greatly different size and shape. In contrast to **1·BF$_4$**, ^{19}F EXSY revealed that neither the larger PF_6^- nor OTf^- encapsulated anion exchanges with solvated anions under the conditions of the NMR measurement (Fig. S27 and S34†). In addition to the resonances that are directly sensitive to the bound guest (*c* and *i*), those corresponding to hydrogens that point outside of the cage cavity (*e* and *b*) also undergo notable changes in chemical shift across the host–guest complexes of **1·X** (Fig. 2b). Based on the data we discuss below, we interpret this as an anion-dependent 'uncoiling/coiling-up' behaviour.[39] This is further supported by the tendency of non-encapsulated anions to influence the chemical shift of proton resonances directly adjacent to the metal centre (in this case, *h* and *g*).[19,48]

In order to gain further insight into the solution-state structure of **1·X**, we examined the host–guest complexes by ^{1}H–^{1}H NOESY. These analyses revealed several intramolecular contacts diagnostic of axial helicity, including a strong inter-ligand correlation between protons *f* and *a* (*e.g.*, Fig. S20†). Cage complexes of larger anions (*e.g.*, SbF_6^-) display an additional NOE contact between protons *i* and *f* of neighbouring ligands (Fig. S39†). The former contact (*f*···*a*), in particular, confirms that the isoquinoline moiety of **L** is closely stacked on top of a neighbouring carbazole ligand backbone – a conformation that could only be afforded by a significantly twisted helical architecture.

The helical structure of **1·X** (X = NO_3^-, ClO_4^-, ReO_4^-, PF_6^-, SbF_6^- and OTf^-) was also examined by Ion-Mobility Mass Spectrometry (IM-MS). The experimental collisional cross section (CCS) values for the $[X@Pd_2\mathbf{L}_4]^{3+}$ species were found to range between 560 ± 10 (**1·BF$_4$**) and 563 ± 17 Å^2 (**1·OTf**) which correlates well to the calculated CCS obtained from their X-ray structures (Table S5.1† and *vide infra*). These CCS values indicate that the cage host maintains its compact helical structure in the solution and gas phase, even when encapsulating anions of notably different size and shape.

Solid-state analysis of 1·X

With MeCN solutions of **1·X** in hand, we grew X-ray quality crystals of each sample (with the exception of **1·NO$_3$**) by slow-vapour diffusion with diisopropyl ether as the antisolvent. **1·BF$_4$**, **1·ClO$_4$** and **1·ReO$_4$** (anions with T_d symmetry) crystallized in the tetragonal space group $P4_2bc$, whilst **1·PF$_6$**, **1·SbF$_6$** and **1·OTf** (O_h and C_{3v} anion symmetry, respectively) crystallized in the monoclinic space group $P2_1/n$. For each structure, the asymmetric unit was occupied by one full molecule of the $Pd_2\mathbf{L}_4$ cage with its respective counter ions and a variable number of solvent molecules. All forms of **1** are stabilised by strong π-stacking interactions between neighbouring ligands and these account for the upfield chemical shift of ligand resonances in the ^{1}H NMR spectra of **1·X** (Fig. 2b). Further inspection of the structures revealed that the azimuthal angle of the cage increases for larger anion guests (*e.g.*, 171.6° and 176.2° for **1·BF$_4$** and **1·SbF$_6$**, respectively – Table ESI 4.3†). This represents the largest axial twist for a M_2L_4 quadruple-stranded metallohelicate reported to date.

For all solid-state structures of **1·X**, one disordered anion was located inside the cage cavity (Fig. 3c), and additional anions sit in close proximity to the Pd^{II} centres. The encapsulated anions are stabilised by multiple weak hydrogen bonds (C–H···X = 2.2–2.5 Å) arising from the carbazole hydrogens that point directly inside the cavity of **1**. For **1·PF$_6$** and **1·SbF$_6$**, the bound anion is tilted by *ca.* 50° with respect to the longest anion axis and Pd(isoquinoline)$_4$ plane, which contrasts with the vertical orientation of PF_6^- in other $Pd_2\mathbf{L}_4$ cages[38] as well as the bound OTf^- in **1·OTf**. The tilted orientation of PF_6^- and SbF_6^- presumably maximises host–guest interactions by orienting the fluoride substituents toward the surrounding hydrogen atoms of the host (also the case for the vertically oriented OTf^- anion).

M_2L_4 cages typically accommodate guests of increasing size by increasing the separation between the metal centres.[39,40,49] In analysing the solid-state structures of **1·X**, we found the opposite trend for the Pd···Pd separation (d_1) with respect to the size and shape of the encapsulated anion. Fig. 3a and b depict how **1** adapts to anions of increasing size. Counter-intuitively, the cage compresses along the Pd–Pd axis for larger anions; d_1 (Pd···Pd distance) = 9.29 Å for **1·BF$_4$** and 8.99 Å for **1·ReO$_4$**. A further decrease of d_1 is observed for **1·PF$_6$** (d_1 = 8.71 Å) followed by a small increase for **1·SbF$_6$** and a much larger increase for the non-globular OTf^- guest (**1·OTf** d_1 = 9.40 Å). Simultaneously, d_2 (average distance between the opposing carbazole N atoms) increases incrementally from **1·BF$_4$** (d_2 = 14.56 Å) to **1·SbF$_6$** (d_2 = 15.12 Fig. 3b). It is worth noting that despite the similar molecular volumes of SbF_6^- and OTf^- (84.9 and 85.4 Å^3 respectively; RB3LYP/6-31g(d), LANL2DZ) **1** closely adapts to their different shape. This is reflected by large differences in d_1 and d_2 when comparing **1·OTf** to **1·SbF$_6$** (+0.59 Å and −0.27 Å, for d_1 and d_2, respectively; Fig. 3b). Combined, this shows that the wide azimuthal angle (or strong helical pitch) of **1** affords

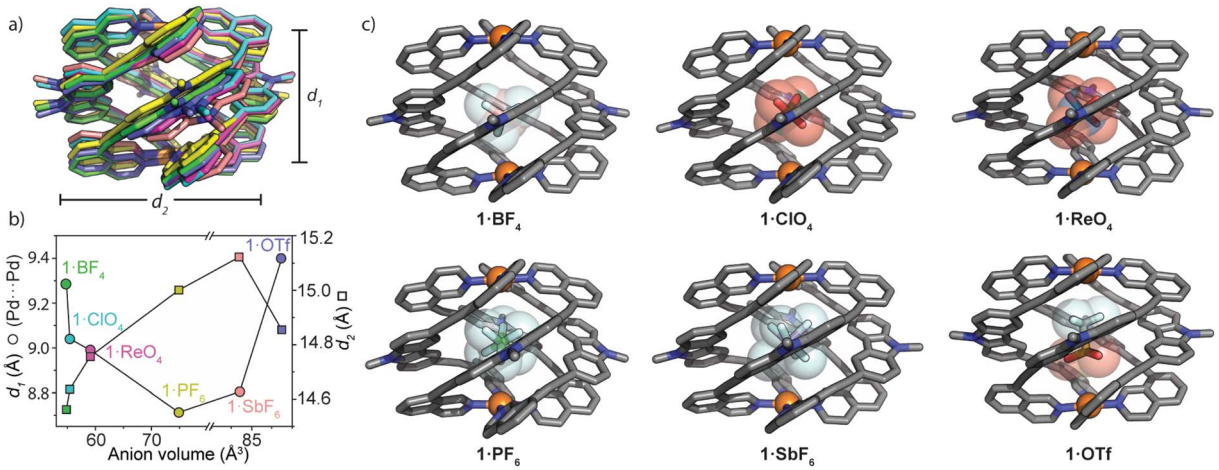

Fig. 3 Solid-state comparison of **1·X**; (a) an overlay of the six X-ray structures of **1** (the structures are centred on Pd1, and counter-ions and hexyl chains are removed for clarity). d_1 = Pd···Pd separation, d_2 = average distance between carbazole-N atoms.; (b) a plot of the solid-state structural parameters obtained from single-crystal X-ray analysis. Anion volumes were calculated by DFT geometry optimizations (RB3LYP; B, O, F, Cl, P, S: 6-31g(d); Re, Sb: LANL2DZ); (c) X-ray crystal structures of **1·X**. Hexyl chains, hydrogen atoms and unbound anions are omitted for clarity.

size and shape adaptability in guest binding, where the cavity trends from a prolate to an oblate shape; as d_1 decreases, d_2 increases. This behaviour enables **1** to alter its cavity volume by up to 18%; for example, the cavity volumes of **1·BF$_4$** and **1·SbF$_6$** are 119 Å^3 and 140 Å^3 respectively, as determined by VOIDOO[50] calculations. These adaptations enable host–guest complexes of **1** to maintain a favourable packing coefficient of 0.55 ± 0.09.[51]

Anion exchange experiments

The versatile anion encapsulation properties of **1** motivated us to investigate anion exchange experiments in CD_3CN solution. A fresh sample of **1·NO$_3$** was titrated with tetrabutylammonium salts of BF_4^-, ClO_4^-, ReO_4^-, PF_6^-, SbF_6^- and OTf^-. In the ^{1}H NMR spectrum of these samples, slow exchange relative to the NMR timescale was observed in each case. Initial calculations revealed that for BF_4^-, $K \approx 10^3$ M^{-1} whilst for the remaining anions, K was estimated to be >10^5 M^{-1}, thus approaching the accuracy limit of K determination by ^{1}H NMR spectroscopy.§

To examine anion exchange more accurately, we turned to Isothermal Titration Calorimetry (ITC). Titrating **1·NO$_3$** with tetrabutyl ammonium salts of BF_4^-, ClO_4^-, and ReO_4^- yielded titration curves consistent with the expected 1 : 1 host–guest binding model (Fig. S52†). The equilibrium constants for anion exchange followed an anion size-dependent trend: $K = 1.9 \times 10^3$ M^{-1} (BF_4^-), 9.2×10^4 M^{-1} (ClO_4^-) and 1.1×10^6 M^{-1} (ReO_4^-) (Fig. 4a and b and Table S3.1†). The thermodynamic data revealed that anion exchange of **1·NO$_3$** with BF_4^- is entropically driven, whilst exchange with ClO_4^- and ReO_4^- is increasingly enthalpically driven (Fig. 4b). Given this, the encapsulated BF_4^- guest may be bound with more degrees of freedom compared to larger ClO_4^- and ReO_4^-. The high enthalpic contributions observed in the exchange of ClO_4^- and ReO_4^- with NO_3^- in **1** point towards a more optimized fit, which presumably maximizes the electrostatic and dispersive interactions in these host–guest complexes.

Monitoring anion exchange of **1·NO$_3$** with PF_6^-, SbF_6^- and OTf^- by ITC was uninformative due to the slow kinetics for the bimolecular exchange processes of these particular anions (*e.g.*, complete exchange with SbF_6^- requires 1.5 h). Time-resolved ^{1}H NMR array experiments revealed the rates of anion exchange to be $OTf^- > PF_6^- > SbF_6^-$; 3.0×10^{-3} s^{-1}, 2.3×10^{-3} s^{-1}, 1.2×10^{-3} s^{-1} respectively (Fig. S53†). In contrast, ITC analysis indicated that anion exchange of **1·NO$_3$** with BF_4^-, ClO_4^- or ReO_4^- is complete within seconds. It is worth noting that the K values for the exchange of nitrate in **1** with polyatomic anions are considerably high (≥10^5 M^{-1} for all

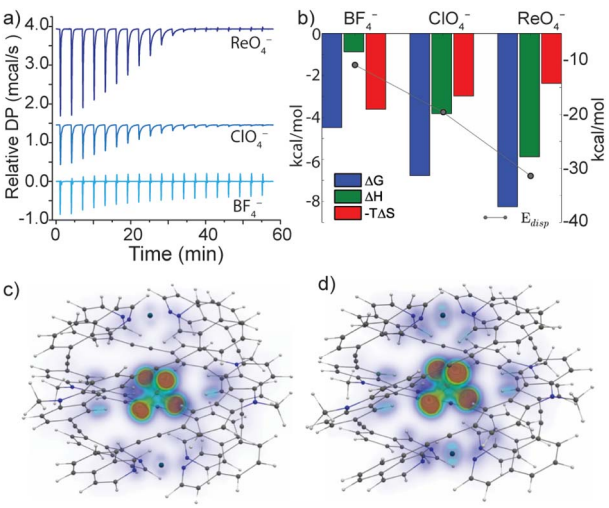

Fig. 4 (a) Relative heat flow produced upon titrating a MeCN solution of **1·NO$_3$** with aliquots of tetrabutyl ammonium BF_4^-, ClO_4^- or ReO_4^- (as determined by ITC analysis); (b) graphical representation of the thermodynamic parameters for guest exchange with a theoretical E_{disp} obtained from electronic structure calculations; calculated dispersion interaction density (VOXEL-DID) of (c) **1·ClO$_4$** gas-phase structure (d) **1·ClO$_4$** solid-state structure.

anions except BF_4^-) compared to other M_2L_4 cages and related cage structures reported in the literature.[19,52,53] For M_2L_4 cages (M = Pd^{II} or Pt^{II}), equilibrium exchange constants for mono-anionic guests in polar solvent are usually in the order of $<10^3$ M^{-1},[39,46] and non-polar solvents, large non-coordinating counter-ions or endohedral binding sites can be employed to further maximize host–guest interactions.[41,54,55] Here, the exceptionally strong anion encapsulation properties of **1** can be credited to the large internal surface area of the tightly-wrapped cavity, which is afforded by the unusually wide azimuthal angles (171–176°).

To investigate the role of London dispersion interactions in the guest binding of **1**, we performed electronic structure calculations on the host–guest complexes examined by ITC (*i.e.*, **1·BF$_4$**, **1·ClO$_4$** and **1·ReO$_4$**; all as 3+ cations with hexyl chains truncated to methyl substituents). All host–guest systems were optimized using the BP-86 [56,57] functional with a def2-SVP[58–61] basis and the D3-correction[D3] including three-body-terms.[62,63] The optimised gas-phase structures were subjected to DF-SCS-LMP2/cc-pVTZ electronic structure calculations and the results were compared to the energies obtained from the corresponding solid-state geometries at the same level of theory.

Indeed, a strong correlation between the measured guest binding enthalpies and calculated dispersion contributions[64–66] was found for both solid-state and gas-phase geometries, where **1** maintains a large contact surface to the bound guest (Fig. 4b–d, S71 and S72†). Additional calculations (DF-SCS-LMP2/VTZ level of theory) revealed that compression of the Pd···Pd axis of **1** is energetically demanding in the absence of a bound guest (Fig. S73†), which leads to the conclusion that dispersion interactions have a strong impact on the guest binding and corresponding structural adaptations of **1**. The trend of increasing dispersion contributions for larger anions is consistent between the solid-state and gas-phase-optimised geometries (Table S5.3†), suggesting that the influence of crystal packing on the solid-state structure of **1** is minimal. This is supported by the fact that **1·BF$_4$**, **1·ClO$_4$** and **1·ReO$_4$** crystallise in the same tetragonal space group with almost identical unit cell dimensions (a, b = 30 Å, c = 29 Å, Table S4.2†).

Helicate/mesocate isomerism of 1

Helicate/mesocate isomerism is prevalent for double and triple-stranded metallohelicates, and control over their selective formation and isolation has been the subject of intense study.[67–69] This in part is motivated by their respective properties; for example, triple-stranded di-ruthenium helicates exhibit selectivity toward certain cancer cells as compared to their mesocate counterparts.[12] For these types of metallohelicates, ligand design (*e.g.*, odd/even spacer length) or steric hindrance can lead to the formation of one isomer over the other.[70,71] In many cases, both helicate and mesocate isomers can form from the same ligand and metal ion and exist either as separable static structures[72] or in dynamic equilibrium;[67,73] the latter is usually the case for helicates based on non-chelated coordination environments with high conformational flexibility (concerning the ligand–metal bonds). However, factors that drive the selective formation of helicates over mesocates remain ill-defined, especially for M_2L_4 quadruple-stranded metallohelicates. This may relate to their acute azimuthal angles (α < 90°), where only subtle structural distortions are required to invert helicity.[74] This means that nearly all so far postulated M_2L_4 mesocates are transient species, rather than isolable ones.[75,76]

In our attempts to grow single crystals of the helical cage **1·NO$_3$**, we were surprised to obtain crystals of a markedly different $[Pd_2L_4]^{4+}$ cage complex (here denoted as **1′**). X-ray analysis revealed that **1′** crystallizes in the orthorhombic space group *Pccn* with half of the Pd_2L_4 cage in the asymmetric unit. In the structure of **1′**, the isoquinoline donors of **L** adopt a *syn* orientation and twist away from the carbazole backbone (giving individual ligands a C_s symmetry) – a conformation which gives rise to a mesocate (in contrast to the C_2-symmetric ligand conformation in the helicates). In this elongated isomer, the Pd···Pd separation is 16.8 Å – which is almost double that of the most contracted form of helical **1·X**. In contrast to the helicate, neighbouring carbazole backbones in mesocate **1′** participate in mutual edge-to-face π-stacking (closest C–H···π contact between two ligand backbones = 3.0 Å) and form the faces of

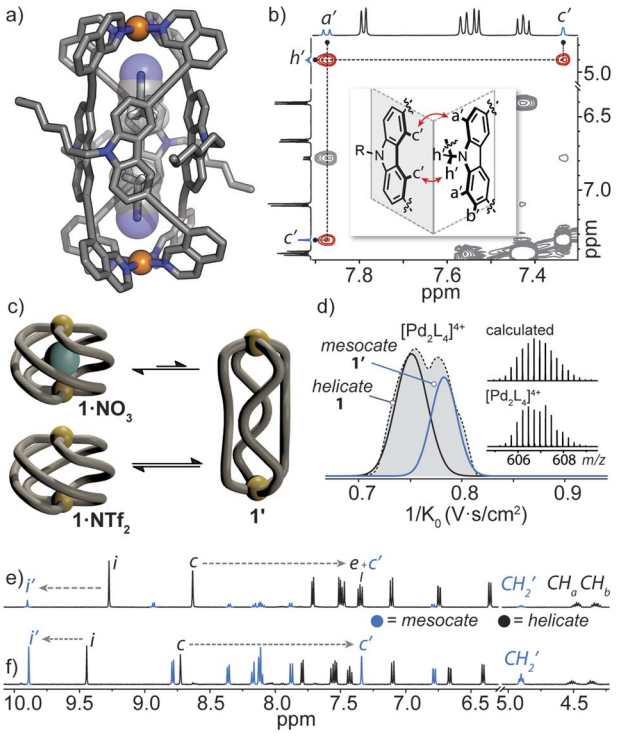

Fig. 5 (a) X-ray structure of mesocate **1′** showing the MeCN solvent guests; (b) ^{1}H–^{1}H NOESY spectrum of **1·NTf$_2$** (R = C_6H_{13}), showing the important contacts in the inset; (c) a schematic of the anion-dependant equilibrium between the helicate **1** and mesocate **1′**; (d); Trapped Ion Mobility (TIMS) mobilogram alongside the measured and calculated isotope pattern of the 4+ species of **1·NTf$_2$**; (e) ^{1}H NMR spectra (500 MHz, CD_3CN) of **1·NO$_3$** after 2 weeks at 25 °C (signal *c′* arising from **1′** overlaps with signals of **1**); (f) **1·NTf$_2$** after two weeks at 25 °C.

the tubular, almost cuboid $Pd_2\mathbf{L}_4$ structure. Instead of encapsulating a NO_3^- counterion, the C_{4h} symmetric mesocate hosts two MeCN solvent molecules (Fig. 5a) that orient their nitrogen atoms toward the opposing Pd^{II} centres. This type of electrostatic interaction has been previously observed for other Pd^{II}-based cages[77] and in the case of **1′**, the MeCN guests are further stabilised by CH–π interactions ($C\text{–}H_{MeCN}\cdots C\text{-}_{carbazole} = 2.66$ Å) inside the aromatic-rich cavity. Although we were not able to obtain an X-ray structure of the expected helical form of **1·NO₃**, the chemical shifts of inward-pointing protons *i* and *c* (Fig. 2a and 5e and f) are consistent with a helically-twisted cage encapsulating a $\mathbf{NO_3}^-$ guest.

To understand the helicate/mesocate isomerism of **1**, we further examined the self-assembly process between **L** and $Pd(NO_3)_2$ in solution. As expected, the ^{1}H NMR spectrum obtained minutes after combining **L** with $Pd(NO_3)_2$ clearly reflects the helical cage species, owing to the characteristic splitting pattern of the diastereotopic N–CH_2 protons (CH_a/CH_b). However, when the CD_3CN solution of **1·NO₃** was allowed to equilibrate over two weeks at room temperature, another set of signals evolved which were assignable to a new Pd^{II} complex of **L** (Fig. 5e, ratio = 1 : 0.15 in favour of **1·NO₃**). The chemical shifts of the newly evolved aromatic resonances appeared downfield compared to **1·NO₃**, with exception of *c* (denoted as *c′*), which appeared significantly upfield (−1.27 ppm). The significant shielding of proton *c′* is in agreement with the X-ray structure of mesocate **1′** as this particular hydrogen points directly toward the π-system of an adjacent carbazole backbone in the mesocate (Fig. 5a and b).

The equilibrium between **1** and **1′** was further investigated by synthesizing **1·NTf₂** (Fig. S42†). We chose NTf_2^- as a counterion because its volumetric size (157 Å^3) is larger than the maximal cavity size of **1** (≤140 Å^3). Thus, an 'empty' form of **1** was prepared by combining **L** with $[Pd(CH_3CN)_4](NTf)_2$ at room temperature. Indeed, the absence of encapsulated NTf_2^- was confirmed by ^{19}F NMR spectroscopy, which showed one isolated signal corresponding to free NTf_2^- present in solution (Fig. S43†). The ^{1}H NMR spectrum of **1·NTf₂** after 5 minutes of mixing the ligand and Pd^{II} salt revealed two sets of signals in a 1 : 0.24 ratio, with the helical, empty form of the cage predominating. After 2 weeks at room temperature, the sample equilibrated to a 1 : 1 ratio (Fig. 5f) of **1** and **1′**. Importantly, ^{1}H–^{1}H NOESY unequivocally confirmed that the second set of signals corresponds to mesocate **1′**. Two characteristic NOE contacts were observed: $a'\cdots c'$ and $c'\cdots h'$ (Fig. 5b and S46†). These contacts originate from the orthogonal relationship of neighbouring carbazole backbones (an arrangement only present in **1′**) and are not observed in the NOESY spectrum of **1** or **L**. The difference in the equilibrium ratios of **1** and **1′** for **1·NO₃** and **1·NTf₂** reveals that the bound NO_3^- anion stabilizes the helicate **1** but is not necessarily required to template it (Fig. 5c). Mesocate **1′** was not observed to encapsulate anions, however, upon addition of a suitable guest (*e.g.*, PF_6^-), the equilibrium shifts in favour of the metallohelicate **1** (Fig. S47†).

Next, Trapped Ion Mobility (TIMS) ESI-MS analysis was carried out on an equilibrated sample of **1·NTf₂** (containing both helicate **1** and mesocate **1′**), in order to gain insight into the gas-phase behaviour of these isomeric structures. Based on previous studies examining structural variations in heteroleptic palladium cages,[78] we anticipated that the drift times of the two isomers of **1** should be resolvable. Indeed, we observed two distinct mobilities corresponding to 4+ ions at 606.7 *m*/*z* (Fig. 5d and S69‡). Derivation of the experimental collisional cross sections (eCCS) for these mobilities revealed that the two 4+ species have an effective area of 605 Å^2 and 631 Å^2, which correspond well to the relative difference between the theoretically determined tCCS values of **1** and **1′** (568.6 Å^2 and 578.9 Å^2, respectively). Thus, the TIMS data confirms the helicate/mesocate pairs (*i.e.*, isomers **1** and **1′**) in the gas phase, suggesting that the MeCN solvent does not play a significant role in templating the formation of **1′**. To investigate this hypothesis further, we examined the formation of **1·BF₄** in DMSO by ^{1}H NMR spectroscopy. In contrast to the exclusive formation of the helicate in MeCN, the ^{1}H NMR spectrum of **1·BF₄** in DMSO revealed the presence of both the helicate and mesocate in a ∼2 : 1 ratio, respectively. Thus, both anionic guests and solvent influence the equilibrium distribution of the helicate/mesocate pair.

Conclusions

In summary, we have presented a comprehensive analysis of the solution state, solid state, and gaseous state structure and host–guest chemistry of the most axially twisted $Pd_2\mathbf{L}_4$ cage reported to date. Through careful ligand design, the helical twist of this $Pd_2\mathbf{L}_4$ cage (azimuthal angle of up to ∼176°) results in exceptionally tight anion binding which is mediated by prolate/oblate cavity size and shape adaptability. Notably, a comparison of six X-ray crystal structures of **1·X** (X = BF_4^-, ClO_4^-, ReO_4^-, PF_6^-, SbF_6^- and OTf^-) provided detailed insights on the compression/decompression of the Pd–Pd distance (d_1), whereby d_1 decreases when larger anions are bound within the cage cavity (with the exception of the non-globular OTf^- guest). In the binding of anions of increasing size, we also observed a subtle increase in the azimuthal angle of the cage host. ^{1}H NMR and ITC analysis revealed the benefit of large axial helicity for **1** by *K* values as high as 10^6 M^{-1} (ReO_4^-) for the bimolecular exchange of NO_3^- with larger anions. This can be attributed to the tightly-wrapped helical cage, which provides a large contact surface that facilitates strong dispersion forces toward the bound anion. In the absence of a suitable guest, 2D NMR, X-ray diffraction and TIM-MS revealed that **1** exists in a well-defined helicate/mesocate equilibrium, and convergence to the helicate is observed in the presence of an appropriate guest.

Although factors such as cavity volume,[79,80] ligand–guest interactions,[55] host asymmetry[35] and metal–metal distance[19] all play a role in the host–guest chemistry of M_2L_4 coordination cages, our work exemplifies how maximising their axial helicity correlates with an exceptionally tight and adaptable binding pocket with a strong affinity toward a range of anionic guests. We anticipate this work will inspire further research into guest recognition/separation by tightly-wrapped helical cage compounds.

Data availability

The synthetic procedures, characterization, spectral data, and additional computational and crystallographic details are available in the ESI.‡ CCDC 1851098–1851104 contain the supplementary crystallographic data for this paper. Additional data is available from the authors upon request.

Author contributions

W. M. B. and G. H. C. conceived the idea. W. M. B. conducted most of the synthesis, characterization, and analysis, and wrote the manuscript. S. H. and C. D. acquired and analysed the IM-MS data. J. J. H. and S. H. solved and refined the X-ray structures. R. A. M. and A. W. performed electronic structure calculations. W. H. performed 2D NMR measurements. G. H. C. managed the project, aided in experimental design, and reviewed the manuscript. All authors provided comments and approved the final version of the manuscript.

Conflicts of interest

There are no conflicts to declare.

Acknowledgements

We thank Dr Andreas Brockmeyer and Dr Petra Janning (Max-Planck Institute for Molecular Physiology, Dortmund) and Dr Holm Frauendorf (Georg-August University Göttingen) for mass spectra measurements. Dyanne Cruickshank from Rigaku Oxford diffraction is thanked for assistance in collecting X-ray data of **1·ReO$_4$**. W. M. B thanks the Alexander von Humboldt Foundation for a postdoctoral fellowship. S. H. thanks the JSPS Program for Advancing Strategic International Networks to Accelerate the Circulation on Talented Researchers. This work has been supported by the Deutsche Forschungsgemeinschaft under priority program SPP 1807 (Control of London Dispersion Interactions in Molecular Chemistry; CL489/3-2 and MA5063/3-2). The European Research Council (ERC Consolidator grant 683083, RAMSES) is also acknowledged for their support. Diffraction data **1·NO$_3$**, **1·PF$_6$**, **1·SbF$_6$**, and **1·OTf** were collected at PETRA III at DESY, a member of the Helmholtz Association (HGF). We thank Anja Burkhardt for assistance at synchrotron beamline P11 (I-20160736).

Notes and references

§ Furthermore, attempts to obtain reliable values of K for **1·X** by ^{1}H NMR spectroscopy were convoluted by the presence of proton resonances of mesocate **1′** which arose in samples of **1·NO$_3$** and **1·BF$_4$** after long periods of equilibration.

1 P. B. Dervan, *Bioorg. Med. Chem.*, 2001, **9**, 2215–2235.
2 A. A. Kornyshev, D. J. Lee, S. Leikin and A. Wynveen, *Rev. Mod. Phys.*, 2007, **79**, 943–996.
3 C. Schmuck, *Angew. Chem., Int. Ed.*, 2003, **42**, 2448–2452.
4 H. Song, M. Postings, P. Scott and N. J. Rogers, *Chem. Sci.*, 2021, **12**, 1620–1631.
5 D. Preston, *Angew. Chem., Int. Ed.*, 2021, **60**, 20027–20035.
6 Y. Ferrand and I. Huc, *Acc. Chem. Res.*, 2018, **51**, 970–977.
7 C. C. Lee, C. Grenier, E. W. Meijer and A. P. H. J. Schenning, *Chem. Soc. Rev.*, 2009, **38**, 671–683.
8 R. P. Megens and G. Roelfes, *Chem.–Eur. J.*, 2011, **17**, 8514–8523.
9 E. Yashima, N. Ousaka, D. Taura, K. Shimomura, T. Ikai and K. Maeda, *Chem. Rev.*, 2016, **116**, 13752–13990.
10 A. C. G. Hotze, B. M. Kariuki and M. J. Hannon, *Angew. Chem., Int. Ed.*, 2006, **45**, 4839–4842.
11 A. D. Richards and A. Rodger, *Chem. Soc. Rev.*, 2007, **36**, 471–483.
12 S. J. Allison, D. Cooke, F. S. Davidson, P. I. P. Elliott, R. A. Faulkner, H. B. S. Griffiths, O. J. Harper, O. Hussain, P. J. Owen-Lynch, R. M. Phillips, C. R. Rice, S. L. Shepherd and R. T. Wheelhouse, *Angew. Chem., Int. Ed.*, 2018, **57**, 9799–9804.
13 D. A. McMorran and P. J. Steel, *Angew. Chem., Int. Ed.*, 1998, **37**, 3295–3297.
14 M. Han, D. M. Engelhard and G. H. Clever, *Chem. Soc. Rev.*, 2014, **43**, 1848–1860.
15 D. Tripathy, A. K. Pal, G. S. Hanan and D. K. Chand, *Dalton Trans.*, 2012, **41**, 11273–11275.
16 M. Yamashina, M. Akita, T. Hasegawa, S. Hayashi and M. Yoshizawa, *Sci. Adv.*, 2022, **3**, e1701126.
17 D. Zhang, T. K. Ronson, Y.-Q. Zou and J. R. Nitschke, *Nat. Rev. Chem.*, 2021, **5**, 168–182.
18 P. J. Steel and D. A. McMorran, *Chem.–Asian J.*, 2019, **14**, 1098–1101.
19 G. H. Clever and P. Punt, *Acc. Chem. Res.*, 2017, **50**, 2233–2243.
20 J. Wang, T. A. Young, F. Duarte and P. J. Lusby, *J. Am. Chem. Soc.*, 2020, **142**, 17743–17750.
21 R. L. Spicer, A. D. Stergiou, T. A. Young, F. Duarte, M. D. Symes and P. J. Lusby, *J. Am. Chem. Soc.*, 2020, **142**, 2134–2139.
22 J. E. M. Lewis, E. L. Gavey, S. A. Cameron and J. D. Crowley, *Chem. Sci.*, 2012, **3**, 778–784.
23 B. Woods, R. D. M. Silva, C. Schmidt, D. Wragg, M. Cavaco, V. Neves, V. F. C. Ferreira, L. Gano, T. S. Morais, F. Mendes, J. D. G. Correia and A. Casini, *Bioconjugate Chem.*, 2021, **32**, 1399–1408.
24 A. Schmidt, V. Molano, M. Hollering, A. Pöthig, A. Casini and F. E. Kühn, *Chem.–Eur. J.*, 2016, **22**, 2253–2256.
25 S. Pullen, J. Tessarolo and G. H. Clever, *Chem. Sci.*, 2021, **12**, 7269–7293.
26 W. M. Bloch and G. H. Clever, *Chem. Commun.*, 2017, **53**, 8506–8516.
27 X. Jing, C. He, L. Zhao and C. Duan, *Acc. Chem. Res.*, 2019, **52**, 100–109.
28 V. Croué, S. Goeb and M. Sallé, *Chem. Commun.*, 2015, **51**, 7275–7289.
29 J. E. M. Lewis, A. Tarzia, A. J. P. White and K. E. Jelfs, *Chem. Sci.*, 2020, **11**, 677–683.
30 D. Ogata and J. Yuasa, *Angew. Chem., Int. Ed.*, 2019, **58**, 18424–18428.

31 A. Tarzia, J. E. M. Lewis and K. E. Jelfs, *Angew. Chem., Int. Ed.*, 2021, **60**, 20879–20887.
32 H. Yu, J. Li, C. Shan, T. Lu, X. Jiang, J. Shi, L. Wojtas, H. Zhang and M. Wang, *Angew. Chem., Int. Ed.*, 2021, **60**, 26523–26527.
33 L. S. Lisboa, J. A. Findlay, L. J. Wright, C. G. Hartinger and J. D. Crowley, *Angew. Chem., Int. Ed.*, 2020, **59**, 11101–11107.
34 M. T. Yong, O. M. Linder-Patton and W. M. Bloch, *Inorg. Chem.*, 2022, **61**, 12863–12869.
35 W. M. Bloch, Y. Abe, J. J. Holstein, C. M. Wandtke, B. Dittrich and G. H. Clever, *J. Am. Chem. Soc.*, 2016, **138**, 13750–13755.
36 S. Löffler, J. Lübben, L. Krause, D. Stalke, B. Dittrich and G. H. Clever, *J. Am. Chem. Soc.*, 2015, **137**, 1060–1063.
37 S. Freye, J. Hey, A. Torras-Galán, D. Stalke, R. Herbst-Irmer, M. John and G. H. Clever, *Angew. Chem., Int. Ed.*, 2012, **51**, 2191–2194.
38 M. Frank, M. D. Johnstone and G. H. Clever, *Chem.–Eur. J.*, 2016, **22**, 14104–14125.
39 P. J. Steel and D. A. McMorran, *Chem.–Asian J.*, 2019, **14**, 1098–1101.
40 J. Lee, S. Lim, D. Kim, O.-S. Jung and Y.-A. Lee, *Dalton Trans.*, 2020, **49**, 15002–15008.
41 D. P. August, G. S. Nichol and P. J. Lusby, *Angew. Chem., Int. Ed.*, 2016, **55**, 15022–15026.
42 J. Xu and K. N. Raymond, *Angew. Chem., Int. Ed.*, 2006, **45**, 6480–6485.
43 S. M. McNeill, D. Preston, J. E. M. Lewis, A. Robert, K. Knerr-Rupp, D. O. Graham, J. R. Wright, G. I. Giles and J. D. Crowley, *Dalton Trans.*, 2015, **44**, 11129–11136.
44 X. Gao, L. Li, W. Sun and P. Chen, *Dalton Trans.*, 2020, **49**, 2843–2849.
45 S. A. Boer and D. R. Turner, *Chem. Commun.*, 2015, **51**, 17375–17378.
46 L.-P. Zhou and Q.-F. Sun, *Chem. Commun.*, 2015, **51**, 16767–16770.
47 W. M. Bloch, J. J. Holstein, W. Hiller and G. H. Clever, *Angew. Chem., Int. Ed.*, 2017, **56**, 8285–8289.
48 J. E. M. Lewis and J. D. Crowley, *Supramol. Chem.*, 2014, **26**, 173–181.
49 J.-Y. Wu, M.-S. Zhong and M.-H. Chiang, *Chem.–Eur. J.*, 2017, **23**, 15957–15965.
50 G. J. Kleywegt and T. A. Jones, *Acta Crystallogr., Sect. D: Biol. Crystallogr.*, 1994, **50**, 178–185.
51 M. Sandro and J. J. Rebek, *Chem.–Eur. J.*, 1998, **4**, 1016–1022.
52 D. Preston, K. M. Patil, A. T. O'Neil, R. A. S. Vasdev, J. A. Kitchen and P. E. Kruger, *Inorg. Chem. Front.*, 2020, **7**, 2990–3001.
53 A. E. Martín Díaz and J. E. M. Lewis, *Front. Chem.*, 2021, **9**, 706462.
54 B. J. J. Timmer and T. J. Mooibroek, *Chem. Commun.*, 2021, **57**, 7184–7187.
55 A. Platzek, S. Juber, C. Yurtseven, S. Hasegawa, L. Schneider, C. Drechsler, K. E. Ebbert, R. Rudolf, Q.-Q. Yan, J. J. Holstein, L. V Schäfer and G. H. Clever, *Angew. Chem., Int. Ed.*, 2022, **61**, e202209305.
56 A. D. Becke, *Phys. Rev. A: At., Mol., Opt. Phys.*, 1988, **38**, 3098–3100.
57 J. P. Perdew, *Phys. Rev. B: Condens. Matter Mater. Phys.*, 1986, **33**, 8822–8824.
58 K. Eichkorn, F. Weigend, O. Treutler and R. Ahlrichs, *Theor. Chem. Acc.*, 1997, **97**, 119–124.
59 F. Weigend and R. Ahlrichs, *Phys. Chem. Chem. Phys.*, 2005, **7**, 3297–3305.
60 F. Weigend, *Phys. Chem. Chem. Phys.*, 2006, **8**, 1057–1065.
61 D. Andrae, U. Häußermann, M. Dolg, H. Stoll and H. Preuß, *Theor. Chim. Acta*, 1990, **77**, 123–141.
62 A. Tkatchenko, D. Alfè and K. S. Kim, *J. Chem. Theory Comput.*, 2012, **8**, 4317–4322.
63 S. Löffler, A. Wuttke, B. Zhang, J. J. Holstein, R. A. Mata and G. H. Clever, *Chem. Commun.*, 2017, **53**, 11933–11936.
64 A. Wuttke and R. A. Mata, *J. Comput. Chem.*, 2017, **38**, 15–23.
65 X. Aniban, B. Hartwig, A. Wuttke and R. A. Mata, *Phys. Chem. Chem. Phys.*, 2021, **23**, 12093–12104.
66 S. Suárez-Pantiga, P. Redero, X. Aniban, M. Simon, C. Golz, R. A. Mata and M. Alcarazo, *Chem.–Eur. J.*, 2021, **27**, 13358–13366.
67 J. Xu, T. N. Parac and K. N. Raymond, *Angew. Chem., Int. Ed.*, 1999, **38**, 2878–2882.
68 K. L. Flint, D. M. Huang, O. M. Linder-Patton, C. J. Sumby and F. R. Keene, *Eur. J. Inorg. Chem.*, 2022, **2022**, e202200225.
69 M. Albrecht, *Chem. Rev.*, 2001, **101**, 3457–3498.
70 M. Albrecht, *Chem.–Eur. J.*, 2000, **6**, 3485–3489.
71 D. J. Cooke, J. M. Cross, R. V Fennessy, L. P. Harding, C. R. Rice and C. Slater, *Chem. Commun.*, 2013, **49**, 7785–7787.
72 Z. Zhang and D. Dolphin, *Chem. Commun.*, 2009, 6931–6933.
73 F. Cui, S. Li, C. Jia, J. S. Mathieson, L. Cronin, X.-J. Yang and B. Wu, *Inorg. Chem.*, 2012, **51**, 179–187.
74 Q. Lin, L. Gao, B. Kauffmann, J. Zhang, C. Ma, D. Luo and Q. Gan, *Chem. Commun.*, 2018, **54**, 13447–13450.
75 S. Carlotto, L. Armelao and M. Rancan, *Int. J. Mol. Sci.*, 2022, **23**, 10619.
76 M. Rancan, J. Tessarolo, A. Carlotto, S. Carlotto, M. Rando, L. Barchi, E. Bolognesi, R. Seraglia, G. Bottaro, M. Casarin, G. H. Clever and L. Armelao, *Cell Rep. Phys. Sci.*, 2022, **3**, 100692.
77 L. Escobar, D. Villarón, E. C. Escudero-Adán and P. Ballester, *Chem. Commun.*, 2019, **55**, 604–607.
78 K. E. Ebbert, L. Schneider, A. Platzek, C. Drechsler, B. Chen, R. Rudolf and G. H. Clever, *Dalton Trans.*, 2019, **48**, 11070–11075.
79 A. P. Birvé, H. D. Patel, J. R. Price, W. M. Bloch and T. Fallon, *Angew. Chem., Int. Ed.*, 2022, **61**, e202115468.
80 J. E. M. Lewis, *Chem. Commun.*, 2022, **58**, 13873–13886.